Gravity Field and Internal Structure of Mercury from MESSENGER

David E. Smith,[1] Maria T. Zuber,[1]* Roger J. Phillips,[2] Sean C. Solomon,[3] Steven A. Hauck II,[4] Frank G. Lemoine,[5] Erwan Mazarico,[1,5] Gregory A. Neumann,[5] Stanton J. Peale,[6] Jean-Luc Margot,[7] Catherine L. Johnson,[8,9] Mark H. Torrence,[10,5] Mark E. Perry,[11] David D. Rowlands,[5] Sander Goossens,[12] James W. Head,[13] Anthony H. Taylor[14]

Radio tracking of the MESSENGER spacecraft has provided a model of Mercury's gravity field. In the northern hemisphere, several large gravity anomalies, including candidate mass concentrations (mascons), exceed 100 milli-Galileos (mgal). Mercury's northern hemisphere crust is thicker at low latitudes and thinner in the polar region and shows evidence for thinning beneath some impact basins. The low-degree gravity field, combined with planetary spin parameters, yields the moment of inertia $C/MR^2 = 0.353 \pm 0.017$, where M and R are Mercury's mass and radius, and a ratio of the moment of inertia of Mercury's solid outer shell to that of the planet of $C_m/C = 0.452 \pm 0.035$. A model for Mercury's radial density distribution consistent with these results includes a solid silicate crust and mantle overlying a solid iron-sulfide layer and an iron-rich liquid outer core and perhaps a solid inner core.

The internal structure of a planet preserves substantial information regarding processes that have influenced thermal and tectonic evolution, and measuring a planet's gravity field provides fundamental information for understanding that body's internal mass distribution. Mapping Mercury's gravity field is consequently a primary objective of the MErcury Surface, Space ENvironment, GEochemistry, and Ranging (MESSENGER) mission (1).

On 18 March 2011, the MESSENGER spacecraft was inserted into a ~12-hour, near-polar orbit around Mercury, with an initial periapsis altitude of 200 km, initial periapsis longitude of 60°N, and apoapsis at ~15,200 km altitude in the southern hemisphere. This highly eccentric orbit permits the mapping of regional gravitational structure

in the northern hemisphere at the maximum resolution of a spherical harmonic model near periapsis but limits the recoverability of the gravity field to long wavelengths at southern latitudes. At the ascending and descending nodes of the orbit (on the equator), the altitude of MESSENGER is about 4900 and 1200 km, respectively.

During the first few weeks after orbit insertion, MESSENGER was tracked extensively at X-band (8 GHz) by stations of NASA's Deep Space Network (DSN). After this initial period of nearly continuous tracking, the typical coverage was less frequent, limiting the number of direct periapsis passages that were observed. We have processed data from 18 March through 23 August 2011, a tracking period that spans more than two Mercury sidereal days (2) (fig. S1). We lim-

ited our analysis to 1-day arcs to reduce the modeling errors from the nonconservative forces, which grow quadratically with time. The aggregated normal equations developed from daily arcs were used to develop solutions of the gravity field of Mercury (2) to degree (l) and order (m) in spherical harmonics, a compromise between data sensitivity and global resolution.

The gravity anomalies and gravitational potential (geoid) of the spherical harmonic solution, here termed HgM002, are depicted in Fig. 1, A and B, respectively. The northern lowlands, ~2 km lower in elevation than surrounding terrain and approximately centered over the north pole (3), correspond to a broad gravity low (Fig. 2). At mid-latitudes, a west-southwest–east-north-east–trending, discontinuous upland that extends for nearly half the circumference of Mercury is

[1]Department of Earth, Atmospheric and Planetary Sciences, Massachusetts Institute of Technology, Cambridge, MA 02139–4307, USA. [2]Planetary Science Directorate, Southwest Research Institute, Boulder, CO 80302, USA. [3]Department of Terrestrial Magnetism, Carnegie Institution of Washington, Washington, DC 20015, USA. [4]Department of Earth, Environmental, and Planetary Sciences, Case Western Reserve University, Cleveland, OH 44106, USA. [5]NASA Goddard Space Flight Center, Greenbelt, MD 20771, USA. [6]Department of Physics, University of California, Santa Barbara, CA 93106, USA. [7]Department of Earth and Space Sciences, University of California, Los Angeles, CA 90095, USA. [8]Department of Earth and Ocean Sciences, University of British Columbia, Vancouver, BC, V6T 1Z4 Canada. [9]Planetary Science Institute, 1700 East Fort Lowell, Suite 106, Tucson, AZ 85719, USA. [10]Stinger Ghaffarian Technologies, Inc., 7701 Greenbelt Rd., Greenbelt, MD 20770, USA. [11]Johns Hopkins University, Applied Physics Laboratory, Laurel, MD 20723, USA. [12]University of Maryland, Baltimore County, Baltimore, MD 21250, USA. [13]Department of Geological Sciences, Brown University, Providence, RI 02912, USA. [14]KinetX, Inc., Tempe, AZ 85284, USA.

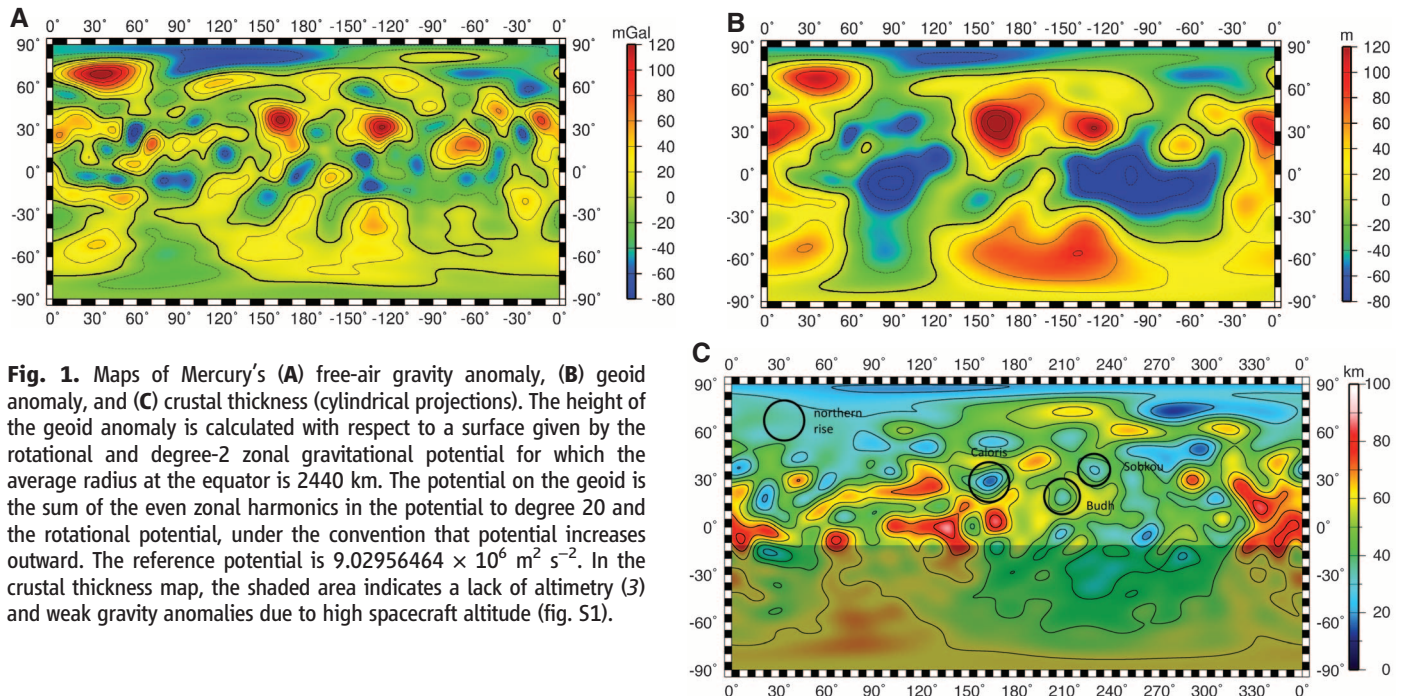*To whom correspondence should be addressed. E-mail: zuber@mit.edu

Fig. 1. Maps of Mercury's (**A**) free-air gravity anomaly, (**B**) geoid anomaly, and (**C**) crustal thickness (cylindrical projections). The height of the geoid anomaly is calculated with respect to a surface given by the rotational and degree-2 zonal gravitational potential for which the average radius at the equator is 2440 km. The potential on the geoid is the sum of the even zonal harmonics in the potential to degree 20 and the rotational potential, under the convention that potential increases outward. The reference potential is 9.02956464×10^6 m^2 s^{-2}. In the crustal thickness map, the shaded area indicates a lack of altimetry (3) and weak gravity anomalies due to high spacecraft altitude (fig. S1).

marked by weakly positive gravity anomalies and thus must be largely balanced at depth by thicker-than-average crust or lower-than-average densities. The gravity field in the northern hemisphere shows several regional anomalies that exceed 100 milli-Galileo (mgal) in amplitude. One such anomaly coincides with Mercury's northern rise, a locally elevated region (centered at 68°N, 33°E) (3) within the northern lowlands and north polar gravity low. Another is associated with the Caloris impact basin (31°N, 160°E), where some of the anomalous mass correlates with and can be attributed to regions of high topography on the basin floor (3). A third positive anomaly is near the Sobkou impact basin (36°N, 226°E), but the gravity anomaly is centered on the southeast rim of that basin, complicating the relation between gravity and topography. Other positive gravity anomalies are not obviously associated with mapped impact basins at the cur-rent resolution of the gravity field. Attempts to resolve mass concentration (or mascon) anomalies similar to those seen at prominent basins on the Moon (4) and Mars (5) from tracking observations during MESSENGER's first two Mercury flybys (6) and the third Mariner 10 flyby (7) have not produced definitive results. From harmonic solution HgM002, the only large, positive free-air gravity anomaly that is spatially well-correlated with an impact basin, the classical definition of a mascon (4), is that associated with the Caloris basin.

The surface that represents Mercury's reference equipotential, or geoid (Fig. 1B), has a dynamic range of 200 m, and its largest anomaly is centered at Caloris. Because the spacecraft altitude over the southern hemisphere is much higher than in the northern hemisphere, the geoid error, projected from the full covariance of the HgM002 solution, is less than 20 m north of the equator but reaches 40 to 50 m in regions of mid- to high latitudes in the southern hemisphere. The presence or absence of large geoid features in the south cannot be confirmed with the present data.

The gravity field has been combined with topography from MESSENGER's Mercury Laser Altimeter (MLA) (3) to produce a map of the crustal thickness of Mercury's northern hemisphere (Fig. 1C). On the basis of surface compositional measurements (8, 9) from MESSENGER's X-Ray Spectrometer (XRS) indicating that the crust is intermediate between basaltic and more ultramafic compositions, as well as melting experiments on candidate mantle compositions consistent with XRS measurements (10), we assume a density contrast between the crust and mantle of 200 kg m^{-3}. On the basis of limits determined from flyby observations of gravity and topography (6, 11) and constraints from tectonic models for the depth extent of faulting (12), we adopt a mean crustal thickness of 50 km. The uncertainty in this mean value represents the largest uncertainty in the crustal thickness model. We also assume uniform values for the densities of the crust and mantle and that all signals in the gravity field not produced by topography are signatures of relief on the crust-mantle boundary. The resulting map of crustal thickness (Fig. 1C) indicates that the crust is generally thicker (50 to 80 km) near the equator and thins toward the north polar region (20 to 40 km), with the regionally thinnest crust located beneath the northern lowlands (3). The Caloris basin overlies an area of locally thin crust, consistent with the interpretation of mascon basins on the Moon (13) and Mars (14) that crustal thinning beneath basins contributes substantially to the observed gravity anomaly. The positive free-air gravity anomaly near Sobkou is associated with an adjacent topographic rise, and the anomaly extends in the directions of both the Sobkou and the Budh (17°N, 208°E) impact basins. If the gravitational effects of topography are removed from the free-air gravity anomaly map, the resulting Bouguer anomaly shows strong positive anomalies centered over the Sobkou and Budh basins and a weaker negative anomaly over the rise, indicating crustal thinning directly beneath the basins and thicker crust beneath the rise (Fig. 1C). Like Caloris, Sobkou and Budh also qualify as mascons on the basis of a crust-mantle boundary that is substantially elevated beneath these basins.

A comparison of gravity anomalies that would result from Mercury's shape alone with the gravity anomalies from the HgM002 solution is made in Fig. 2. High-standing terrain borders many parts of the northern lowlands (3), as is also evident in the broader-scale view of the equivalent gravity field (Fig. 2A). Mild gravity anomalies in this region (Fig. 2B) suggest a high degree of interior mass compensation. By contrast, the northern rise has a gravity anomaly nearly as strong as that due to shape alone (~150
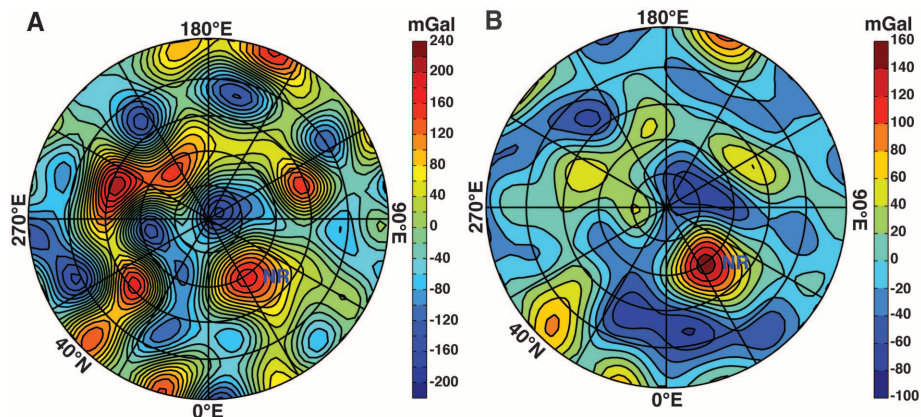

Fig. 2. (A) The radial component of the gravitational acceleration vector resulting from a 20 by 20 spherical harmonic expansion of Mercury's shape (3) given a density of upper crustal material of 3100 kg m^{-3}. Results are shown in a polar stereographic projection north of 40°N. NR indicates the location of the northern rise. (B) The radial component of the gravitational acceleration vector resulting from the 20 by 20 HgM002 spherical harmonic gravity solution. In both plots, the solution shown has been limited to spherical harmonic terms with degrees 6 and greater to emphasize local- to regional-scale anomalies. The calculation demonstrates that gravity and shape are correlated and that the topography, except for the northern rise, is approximately compensated.

Table 1. Normalized* low-degree gravity coefficients in the HgM002 gravity model for Mercury.

Parameter	Value	Uncertainty†	Comments
GM, km^3 s^{-2}	22031.780	±0.02	No significant difference from HgM001.
$C_{20} \times 10^{-5}$	−2.25	±0.01	~20% smaller than Mariner 10 estimate of (−2.68 ± 0.89) × 10^{-5}.
$C_{21} \times 10^{-8}$	−4.64	±5	Consistent with coalignment of gravity field and angular momentum vector.
$S_{21} \times 10^{-8}$	1.35	±5	
$C_{22} \times 10^{-5}$	1.253	±0.01	Ratio of S_{22}/C_{22} is small, indicating that the equatorial major axis of the gravity field is aligned with Mercury's "hot-pole" longitudes.
$S_{22} \times 10^{-5}$	0.005	±0.01	
$C_{30} \times 10^{-6}$	−4.49	±0.3	Negative value indicates that a periapsis over the south pole is needed for a stable spacecraft orbit about Mercury.
$C_{40} \times 10^{-6}$	−6.5	±0.8	

*Normalizations follow those of Kaula (29).   †Uncertainties are best estimates rather than formal errors.

versus ~170 mGal), indicating little mass compensation and a thick lithosphere. We have estimated the thickness, T_e, of the effective elastic lithosphere beneath the northern rise by assuming that partial compensation takes place at the crust-mantle boundary and then finding model solutions that best fit the gravity anomaly in terms of crustal and elastic lithosphere thicknesses (Fig. 2). Over a crustal thickness range of 25 to 100 km, T_e is 70 to 90 km, and the downward flexural deflection of the crust-mantle boundary is minor (3 to 5 km), consistent with the lack of a discernible crustal thickness anomaly at the northern rise (Fig. 1C). An elastic lithosphere is a surrogate for one with more complex temperature-dependent strength, but temperatures at a given depth in the lower crust and uppermost mantle vary approximately inversely with T_e. The northern rise, part of the northern smooth plains volcanic complex (15), has been estimated from its impact crater size-frequency distribution to have a surface that formed ~3.7 to 3.8 billion years ago (Ga), substantially younger than that of the surrounding heavily cratered highlands (16). The greater level of apparent mass compensation of the highlands will yield, under similar assumptions, a thinner elastic lithosphere and higher crustal and mantle temperatures at the time of formation than the northern rise. The inference that Mercury's interior generally cooled with time is in keeping with thermal evolution models for the terrestrial planets. T_e estimates for Mars derived from gravity-topography relations for regions with ages of major topographic features similar to that of the northern rise, in contrast, are considerably smaller (17).

The major parameters of gravity field solution HgM002, including the product of the gravitational constant and Mercury's mass (GM), are given in Table 1. The GM value is close to that given by the most recent previous model of Mercury's gravitational field (HgM001), derived solely from the tracking of MESSENGER during its first two near-equatorial flybys (6).

The covariance matrix of solution HgM002 was used to generate clone models of the gravity field in order to analyze the error characteristics for the degree-2 coefficients and C_{30} (2) (fig. S5). The harmonic coefficients C_{20} and C_{22} are tightly bounded with small relative uncertainties, and C_{21} and S_{21} are small (Table 1).

The C_{20} and C_{22} terms provide important constraints on the interior structure of Mercury because they are directly relatable to the radial distribution of density. Earth-based radar measurements of Mercury's pole position confirm that the planet occupies a Cassini state in which the axis of rotation remains coplanar with the orbit normal and the normal to the Laplace plane as the spin vector and the orbit normal precess together about the latter with an ~300,000-year period (18). Radar observations also show that the amplitude of the 88-day physical libration in longitude is so large that the mantle and crust must be librating independently of the core (18).

This state allows the determination of Mercury's normalized polar moment of inertia, C/MR^2, where R is Mercury's mean radius, and a measurement of the ratio of the polar moment of inertia C_m of the solid outer portion of the planet (6, 18) to that of the entire planet (19, 20). The values of C_{20} and C_{22} (Table 1), combined with Earth-based radar measurements of the amplitude of Mercury's forced libration and obliquity (18) and ancillary data on the precession rate and pole position (21), provide the information necessary to estimate C/MR^2 and C_m/C. A libration amplitude of 35.8 ± 2 arcseconds and a slightly revised obliquity value of 2.06 ± 0.1 arcmin (22) yields internal structure parameters $C/MR^2 = 0.353 \pm 0.017$ and $C_m/C = 0.452 \pm 0.035$.

Resulting moment of inertia parameters for more than 1 million Monte Carlo models that include a silicate crust and mantle, as well as an Fe-rich core that may contain solid and liquid layers are shown in Fig. 3. These models are constrained only by the mean radius (2440 km) and bulk density of Mercury [5430 kg m^{-3}, e.g., (23)]. Comparison of the internal structure models with the measured moment of inertia parameters indicates that the outer radius of the liquid portion of the core under the adopted modeling assumptions is 2030 ± 37 km (1 SD), and the density of the outer shell overlying the liquid core is 3650 ± 225 kg m^{-3}. The procedure does not provide a size estimate for any solid inner component of the core.

The large average bulk density inferred for Mercury's solid outer shell is surprising given that measurements by the MESSENGER XRS determined an upper bound on the average surface abundance of Fe of ~4 weight percent (8). Although uncertainty in the density of the solid shell permits a wide range of possibilities, the nominal value provides an important constraint on the planet's bulk composition. The low Fe abundance in volcanic rocks at Mercury's surface suggests that Mercury's silicate mantle is also low in iron and cannot account for the outer shell density. Relatively low surface abundances

of Ti and Al (8) are also inconsistent with substantial amounts of such high-density mantle minerals as ilmenite and garnet. A deeper reservoir of high-density material is therefore needed to account for the large solid-shell density and moment of inertia. One possibility is a dense silicate layer, possibly Fe-bearing, that has not substantively participated in the generation of Mercury's crust.

Alternatively, Mercury may have a solid layer of FeS at the top of the core. The highly reducing chemical conditions implied for Mercury's precursory materials by the low Fe and high S content of surface rocks (8, 9) suggest that Mercury's core likely contains substantial Si as well as S (24). Fe-S-Si alloys are subject to liquid immiscibility at pressures less than ~15 GPa (25), resulting in the buoyancy segregation of S-rich liquids at the top of the core. The density of solid FeS is sufficiently low that for a broad range of conditions the solid form would likely remain at the top of the core. There is a strong, albeit poorly constrained, trade-off between the thickness of a basal solid FeS layer and the density of the silicate mantle, although the basal layer could be a few tens of kilometers to as much as ~200 km in thickness. The thickness of the outer silicate portion of the planet would, under this interpretation, be thinner than the nominal 410-km depth to the solid-liquid boundary. A solid FeS layer at the base of the mantle would place strong constraints on the present thermal structure of Mercury. Moreover, a static, electrically conducting layer at the top of the core would act to decrease the overall strength of the field observable at or above the planetary surface and would attenuate harmonic components of the magnetic field increasingly strongly with increasing degree (26).

The gravity field results point to a much different interior structure for Mercury from that heretofore anticipated and from those of the other terrestrial planets. These results will require reconsideration of models for Mercury's interior thermal (27) and tectonic (28) evolution.
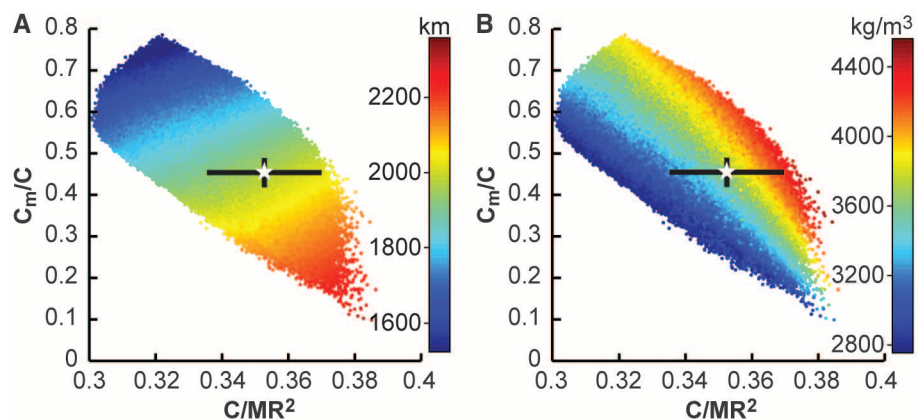

Fig. 3. (A) Outer radius of Mercury's liquid core. (B) Average density of the solid shell that overlies the liquid core. The stars represent the central values for C/MR^2 and C_m/C, and the black bars denote $\pm$ 1 SD.

References and Notes

1. S. C. Solomon, R. L. McNutt Jr., R. E. Gold, D. L. Domingue, *Space Sci. Rev.* **131**, 3 (2007).
2. Materials and methods are available as supporting material on *Science* Online.
3. M. T. Zuber et al., *Science* **336**, 217 (2012); 10.1126/science.1218805.
4. P. M. Muller, W. L. Sjogren, *Science* **161**, 680 (1968).
5. D. E. Smith et al., *J. Geophys. Res.* **98**, 20871 (1993).
6. D. E. Smith et al., *Icarus* **209**, 88 (2010).
7. J. D. Anderson, J. Palguta, G. Schubert, Abstract P41A-1572, paper presented at the American Geophysical Union Fall Meeting, San Francisco, CA, 5 to 9 December 2011.
8. L. R. Nittler et al., *Science* **333**, 1847 (2011).
9. L. R. Nittler et al., Abstract 142-3, paper presented at the Geological Society of America Annual Meeting, Minneapolis, MN, 9 to 12 October 2011.
10. B. Charlier, T. L. Grove, M. T. Zuber, *Lunar Planet. Sci.* **43**, abstract 1400 (2012).
11. M. T. Zuber et al., *Science* **321**, 77 (2008).
12. F. Nimmo, T. R. Watters, *Geophys. Res. Lett.* **31**, L02701 (2004).
13. G. A. Neumann, M. T. Zuber, D. E. Smith, F. G. Lemoine, *J. Geophys. Res.* **101** (E7), 16841 (1996).
14. M. T. Zuber et al., *Science* **287**, 1788 (2000).
15. J. W. Head et al., *Science* **333**, 1853 (2011).
16. R. G. Strom, G. Neukum, in *Mercury*, F. Villas, C. R. Chapman, M. S. Matthews, Eds. (Univ. of Arizona Press, Tucson, 1988), pp. 363–373.
17. P. J. McGovern et al., *J. Geophys. Res.* **109**, E07007 (2004).
18. J.-L. Margot, S. J. Peale, R. F. Jurgens, M. A. Slade, I. V. Holin, *Science* **316**, 710 (2007).
19. S. J. Peale, *Nature* **262**, 765 (1976).
20. S. J. Peale, R. J. Phillips, S. C. Solomon, D. E. Smith, M. T. Zuber, *Meteorit. Planet. Sci.* **37**, 1269 (2002).
21. M. Yseboodt, J.-L. Margot, *Icarus* **181**, 327 (2006).
22. J.-L. Margot, S. Padovan, S. J. Peale, S. C. Solomon, Abstract P41A-1573, paper presented at the American Geophysical Union Fall Meeting, San Francisco, CA, 5 to 9 December 2011.
23. S. A. Hauck II, S. C. Solomon, D. A. Smith, *Geophys. Res. Lett.* **34**, L18201 (2007).
24. V. Malavergne, M. J. Toplis, S. Berthet, J. Jones, *Icarus* **206**, 199 (2010).
25. G. Morard, T. Katsura, *Geochim. Cosmochim. Acta* **74**, 3659 (2010).
26. U. R. Christensen, *Nature* **444**, 1056 (2006).
27. S. A. Hauck II, A. J. Dombard, R. J. Phillips, S. C. Solomon, *Earth Planet. Sci. Lett.* **222**, 713 (2004).
28. M. T. Zuber et al., *Icarus* **209**, 88 (2010).
29. W. M. Kaula, *Theory of Satellite Geodesy* (Blaisdell, Waltham, MA, 1966).

Topography of the Northern Hemisphere of Mercury from MESSENGER Laser Altimetry

Maria T. Zuber,[1]* David E. Smith,[1] Roger J. Phillips,[2] Sean C. Solomon,[3] Gregory A. Neumann,[4] Steven A. Hauck II,[5] Stanton J. Peale,[6] Olivier S. Barnouin,[7] James W. Head,[8] Catherine L. Johnson,[9] Frank G. Lemoine,[4] Erwan Mazarico,[1,4] Xiaoli Sun,[4] Mark H. Torrence,[4,10] Andrew M. Freed,[11] Christian Klimczak,[3] Jean-Luc Margot,[12] Jürgen Oberst,[13] Mark E. Perry,[7] Ralph L. McNutt Jr.,[7] Jeffrey A. Balcerski,[5] Nathalie Michel,[5] Matthieu J. Talpe,[1] Di Yang[1]

Laser altimetry by the MESSENGER spacecraft has yielded a topographic model of the northern hemisphere of Mercury. The dynamic range of elevations is considerably smaller than those of Mars or the Moon. The most prominent feature is an extensive lowland at high northern latitudes that hosts the volcanic northern plains. Within this lowland is a broad topographic rise that experienced uplift after plains emplacement. The interior of the 1500-km-diameter Caloris impact basin has been modified so that part of the basin floor now stands higher than the rim. The elevated portion of the floor of Caloris appears to be part of a quasi-linear rise that extends for approximately half the planetary circumference at mid-latitudes. Collectively, these features imply that long-wavelength changes to Mercury's topography occurred after the earliest phases of the planet's geological history.

The topography of a planet provides fundamental information about its internal structure and geological and thermal evolution. Ranging observations made from orbit by the Mercury Laser Altimeter (MLA) (*1*) on the MErcury Surface, Space ENvironment, GEochemistry, and Ranging (MESSENGER) (*2*) spacecraft have provided a precise, geodetically referenced topographic model of the northern hemisphere of the planet as well as a characterization of slopes and surface roughness over a range of spatial scales.

From MESSENGER's eccentric, near-polar orbit (*2*), the MLA (*3*) illuminates surface areas averaging between 15 and 100 m in diameter, spaced ~400 m apart along the spacecraft ground track. The range from the spacecraft to the surface is converted to a measurement of radius from the planet's center of mass via the deter-

mination of MESSENGER's orbit. Radius is then converted to topography (Fig. 1A) by subtracting the radius of the gravitational equipotential or geoid obtained from Doppler tracking of MESSENGER (*4*). The radial precision of individual measurements is <1 m, and the accuracy with respect to Mercury's center of mass is better than 20 m (Table 1). MLA can successfully range at distances up to 1500 km from Mercury's surface when operating at nadir, and from ~1000 km at angles up to 40° from the vertical (*5*). As of 2 December 2011, more than 4.3 million independent measurements of surface elevation had been obtained.

Elevations in Mercury's northern hemisphere exhibit an approximately symmetric, unimodal hypsometric distribution and a dynamic range of 9.85 km (Fig. 2), considerably less than the global dynamic range for the Moon (19.9 km)

or Mars (30 km) (*6*, *7*). Mercury contains numerous large impact structures (*8*, *9*) that influence the hemispheric shape but do not markedly affect the hypsometry.

Mercury's high bulk density, presumably the result of an iron-rich core that constitutes an unusually large mass fraction of the planet (*10*), yields a surface gravitational acceleration comparable to that of Mars for a body intermediate in size between Mars and the Moon. For at least some topography-producing forces, a higher gravitational acceleration results in less variation in elevation, which can account for the difference in topographic dynamic range between Mercury and the Moon. However, Mercury's shallow core-mantle boundary, at a depth of <400 km below the surface (*4*), could have affected viscous flow in Mercury's mantle and may have influenced the growth and relaxation of the largest structures (*11*). Shield-building volcanism and large-scale extension contribute substantially to the dynamic range of topography on Mars but have no evident counterparts on Mercury. Indeed,

[1]Department of Earth, Atmospheric and Planetary Sciences, Massachusetts Institute of Technology, Cambridge, MA 02139, USA. [2]Planetary Science Directorate, Southwest Research Institute, Boulder, CO 80302, USA. [3]Department of Terrestrial Magnetism, Carnegie Institution of Washington, Washington, DC 20015, USA. [4]NASA Goddard Space Flight Center, Greenbelt, MD 20771, USA. [5]Department of Earth, Environmental and Planetary Sciences, Case Western Reserve University, Cleveland, OH 44106, USA. [6]Department of Physics, University of California, Santa Barbara, CA 93106, USA. [7]Johns Hopkins University Applied Physics Laboratory, Laurel, MD 20723, USA. [8]Department of Geological Sciences, Brown University, Providence, RI 02912, USA. [9]Department of Earth and Ocean Sciences, University of British Columbia, Vancouver, BC V6T 1Z4, Canada. [10]Stinger Ghaffarian Technologies Inc., 7701 Greenbelt Road, Greenbelt, MD 20770, USA. [11]Department of Earth and Atmospheric Sciences, Purdue University, West Lafayette, IN 47907, USA. [12]Department of Earth and Space Sciences, University of California, Los Angeles, CA 90095, USA. [13]Institute of Planetary Research, German Aerospace Center, Berlin D-12489, Germany.

*To whom correspondence should be addressed. E-mail: zuber@mit.edu